J. Fluid Mech. (1985), *vol.* 160, *pp.* 235–256
Printed in Great Britain

Unsteady separation in a boundary layer produced by an impinging jet

By NORBERT DIDDEN† and CHIH-MING HO
Department of Aerospace Engineering, University of Southern California, Los Angeles, California, 90089-1454

(Received 24 April 1984 and in revised form 6 May 1985)

A vortex-induced unsteady separation was investigated experimentally in the laminar boundary layer produced by an axisymmetric jet impinging normally onto a flat plate. By forcing the air jet, primary ring vortices were periodically generated in the jet shear layer. Phase-locked flow visualization showed that the wall-jet boundary layer separated periodically and evolved into a secondary vortex counter rotating with respect to the primary vortex. The unsteady separation is induced by the primary vortex and moves *downstream* in the radial mean-flow direction. Phase-averaged hot-wire measurements using a parallel-wire sensor in the vicinity of the unsteady separation provided data for locating the onset of separation in space and time. The data revealed that the unsteady separation originated from a *local shear layer* which was initiated by *the unsteady adverse pressure gradient* produced by the primary vortex.

1. Introduction

Unsteady separation is an important feature of many flows. For example global aerodynamic properties such as the lift and drag (McCroskey, Carr & McAlister 1975) can be stronger affected by the local unsteady separation in the boundary layer. More than two decades ago the point of vanishing wall shear stress, which defines the separation point in steady flow over fixed walls (Prandtl 1904), was found to be insufficient for separation in unsteady flows (Sears 1956; Rott 1956; Moore 1958). Sears (1956) postulated that unsteady separation should occur at a point within the boundary layer where both shear stress and velocity vanish in a frame of reference moving with the separation point. This criterion became known as the MRS condition (figure 1). The drawback is that the velocity of the separation point is unknown. Hence, it is difficult to locate the separation point.

Sears & Telionis (1971) were able for the first time to investigate numerically the upstream-moving separation in a boundary layer. They found that the separation point could be identified by a singular point in the solution of the boundary-layer equation. Williams (1977) reviewed the evidence for the validity of the MRS condition in several upstream-moving separation cases; the available numerical techniques, however, could not yield solutions for the case of *downstream*-moving separation, which is considered here. Van Dommelen & Shen (1982) used a new approach, the Lagrangian technique, to study the upstream-moving separation of the flow about an impulsively started cylinder. They demonstrated that the shedding of boundary-layer vorticity into the free stream at a singular point satisfied the MRS condition.

† Present address: Institut für Meereskunde an der Universität Kiel, 23 Kiel 1, F. R. Germany.

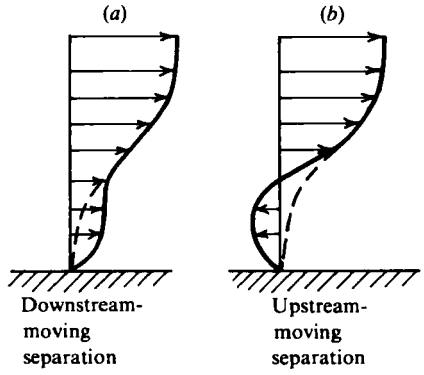

FIGURE 1. Velocity profiles in separated flows. ---, steady separation velocity profile; ——, unsteady separation velocity profile.

Cebeci (1982) used a different technique: the results agreed very well with Van Dommelen & Shen's calculation.

Very few experimental studies on unsteady boundary layers are available (Parikh *et al.* 1981; Cousteix, Houdeville & Javelle 1981). Investigations on unsteadily separated boundary layers are even more scarce and mostly are upstream-moving turbulent-separation cases (Simpson 1981). In laminar unsteady separation studies, the search for the separation criterion has been the main task (Wang 1979; Williams 1977; Telionis 1981). Despard & Miller (1971) investigated the laminar boundary layer in an oscillating flow with adverse pressure gradient and showed that zero wall shear stress and flow reversal occurred periodically over some distance upstream of separation. They suggested that the separation point coincided with the first downstream location at which the flow was reversed throughout the entire cycle of oscillation. Koromilas & Telionis (1980) studied unsteady separation in a water channel by impulsively changing the pressure gradient. Their flow visualization revealed the existence of a saddle point, which supported the MRS criterion.

Unsteady separation also occurs in flows with concentrated vortices moving close to a wall. This was observed by Harvey & Perry (1971) in the case of a trailing wing-tip vortex which approached the ground and then lifted off after it reached a minimum distance. This 'rebounding effect' was found to be due to a secondary vortex originating from a separation of the boundary layer between the vortex and the ground. The same effect is present if a ring vortex approaches a wall normal to its propagation. The secondary-vortex formation was clearly shown by Magarvey & McLatchy (1964) who did not comment on separation however. Visual studies of impinging ring vortices are also reported by Cerra & Smith (1980), Schneider (1980) and Liang, Falco & Bartholomew (1983). The evolution of the boundary layer induced by a single straight vortex moving at constant height above a plate was theoretically considered by Walker (1978). A closed recirculation region (in a frame moving with the vortex) appeared within the boundary layer slightly downstream of the vortex. As the recirculation region increased in size, the rapid thickening of the boundary layer indicated separation. Calculations along the same lines for impinging ring vortices by Doligalski (1980) showed qualitatively the same flow pattern.

The unsteady separation of the laminar boundary layer considered in the present study was induced by impinging ring vortices. In our study, however, the periodically produced ring vortices were embedded into the mean flow of an impinging jet. On

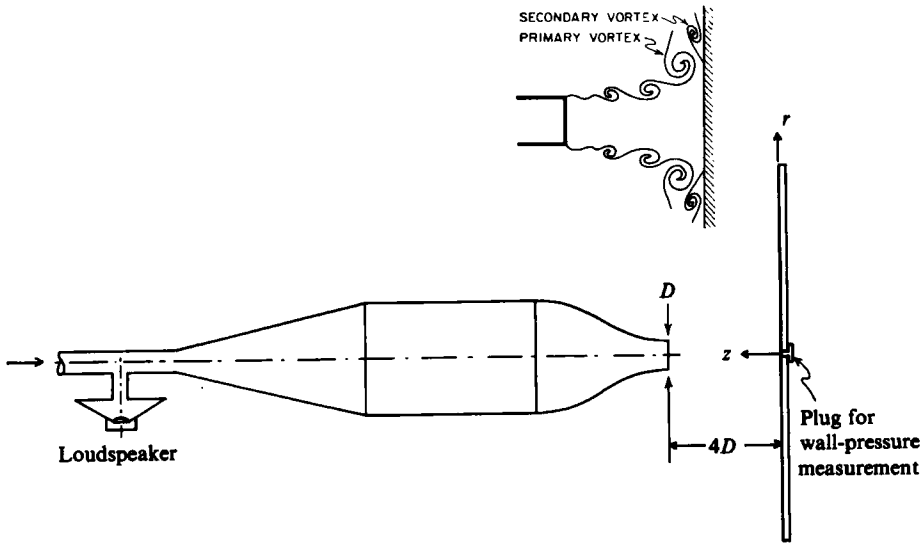

FIGURE 2. Schematic diagram of air-jet facility with impingement plate.

the plate, each ring vortex spread radially and travelled along the plate in the boundary layer of the wall jet. Flow visualization indicated a periodic separation of the laminar boundary layer. The separation region moved downstream with each primary ring vortex and evolved into a secondary ring vortex of opposite rotation. The velocity field and the wall-pressure distribution were surveyed in detail. The data validated the MRS criterion and brought many important physical processes to light. The unsteady pressure gradient was identified as the mechanism initiating the separation and viscous–inviscid interaction was shown to play the main role in the unsteady separation process.

2. Facility and instrumentation

2.1. *Impinging jet*

The jet facility shown in figure 2 was driven by an axial blower and consisted of a stagnation chamber and a nozzle of $D = 3.81$ cm (1.5 in.) diameter with a contraction ratio of 16:1. Upstream of the diffuser a speaker activated by a sine-function generator modulated the mean jet flow and enhanced the naturally occurring ring vortices in the jet shear layer. The measurements were performed at an exit velocity of $U_0 = 7.5$ m/s corresponding to a Reynolds number of 19000, based on the diameter and the jet exit velocity. At 4 diameters downstream of the jet exit, i.e. upstream of the end of the potential core, a 50×50 cm Plexiglas impingement plate was mounted perpendicular to the jet axis. A cylindrical coordinate system centred at the stagnation point on the plate was used: r and z were the radial and axial coordinates (z measured the distance from the wall). The corresponding radial and axial velocities were u and v.

2.2. *Flow visualization and forcing of the jet*

For flow visualization smoke streaklines were produced at two points in the shear layer close to the nozzle. Oil was continuously supplied through a thin cotton thread

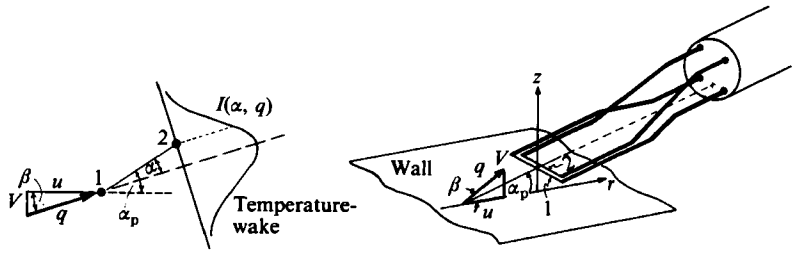

FIGURE 3. Parallel-wire probe for two-component velocity measurements: (*a*) thermal wake of constant-temperature wire 1 at the location of temperature-sensing wire 2; (*b*) sensor geometry and orientation.

and vaporized from the tip of a heated wire. A third streakline was produced at the plate near the stagnation point. The smoke was entrained into the boundary layer and indicated the formation of the secondary vortex. Stroboscopic light synchronized with the forcing signal was used to illuminate the flow. The smoke pattern showed that the row of ring vortices was sufficiently coherent and repeatable. With a stroboscope frequency slightly different from the forcing frequency a 'slow motion' sequence of the vortex roll-up and downstream evolution could be observed. This method provided a helpful tool in finding a combination of jet velocity, forcing frequency and forcing amplitude, for which spatial jitter and phase fluctuations of the primary vortices were minimized. A forcing frequency of $f = 70$ Hz was used. From flow visualization, the row of ring vortices generated at 70 Hz was found to be most stable at an exit velocity of $U_0 = 7.5$ m/s. This frequency corresponds to a Strouhal number, based on the nozzle diameter, of $St = 0.35$, which is close to the values found by several investigators for the jet-preferred mode of an unforced jet (Gutmark & Ho 1983). 70 Hz was also the organ-pipe resonance frequency of the jet facility. The r.m.s. forcing level was chosen to be $0.18U_0$.

2.3. *Hot-wire anemometry*

A large magnitude of the v-velocity is one of the main characteristics of unsteady separation. Hence both velocity components u and v must be measured or, alternatively, both the magnitude and the direction of the velocity vector. In the present experiment the typical boundary-layer-displacement thickness was of the order of a few mm. Thus a conventional X-wire probe cannot be applied. Another type of hot-wire probe (figure 3) with a sensor consisting of two parallel wires (PW probe) was used. The PW probe was first reported by Walker & Bullock (1972) and further developed by Dr J. H. Haritonidis at U.S.C. The first wire was operated in a constant-temperature mode and measured the magnitude q of the velocity vector. The second wire was operated as a 'cold wire' in a constant-current mode at a very low current (here 0.3 mA), and thus was sensitive to temperature only. The second wire detected the temperature in the laminar wake of the first wire. The anemometer circuit was designed to obtain an output voltage T proportional to the temperature difference between the wake and ambient flow. This output voltage was a unique function of α and q, and was determined by angle calibration at the jet nozzle for several velocities q in the range 1–10 m/s. An analytical function suggested by Dr Haritonidis was used to fit the calibration data. Then for any unknown flow field, q and T were obtained from the first and second wire respectively. The angle $\alpha(T, q)$ could then be computed from the calibration function.

The PW probe was made by soldering platinum wires to the tips of jeweller broaches of 0.06 mm diameter (figure 3). The first wire, of diameter $d_1 = 2.5$ μm and length 1.25 mm, was operated at 20 % overheat ratio. The frequency response was flat from d.c. to 20 kHz. The second wire had a smaller diameter in order to achieve a reasonable frequency response. For a constant-current anemometer the frequency response has a first-order low-pass filter characteristic (Weidman & Browand 1975). For the 1.25 μm diameter wire (length 0.9 mm) used here the corner frequency at the −3 dB point was typically 700 Hz, slightly dependent upon the wake temperature. A digital frequency compensation was applied to extend the frequency response (see §3.1). The spacing between the parallel wires was $28d_1$ (70 μm). For small velocities $q \leqslant 4$ m/s the temperature wake was wide enough to allow an angle calibration for angles of α from 0° to 80°. With increasing velocity the width of the wake decreased and for $q = 10$ m/s the maximum calibration angle was about 40°. The calibration error $\Delta\alpha$, i.e. the deviation of α from the angle computed from the best-fitting calibration function $T(\alpha, q)$, was largest at low velocities and high angles ($\Delta\alpha = 5°$ at 1 m/s and $\alpha = 80°$). At velocities above 4 m/s and angles between 10° and 50° the error was less than 1°.

In the velocity range 3–10 m/s the slope of the wake temperature distribution $T(\alpha, q)$ reached a maximum at about $\alpha = 30°$. Therefore, measurements in the wall jet were performed at a fixed probe angle $\alpha_p = 30°$ between the plane of the parallel wires and the wall, resulting in an optimum angle sensitivity at small flow angles $\beta = \alpha_p - \alpha$. Since the temperature wake was symmetric about $\alpha = 0$, the PW-probe measured the absolute value of β only. Thus, for a calibration range $\alpha \leqslant 80°$, flow angles β from −50° to 30° were measured without ambiguity at one side of the wake. For flow angles $\beta = \alpha_p - \alpha > 30°$ the computed angle α was taken to be negative. In the wall jet this only occurred at some locations over very short fractions of the period. It was easily detectable owing to the peculiar shape of the time traces $\beta(t)$ and therefore could be taken into account.

2.4. *Pressure transducer*

The mean and fluctuating wall pressure were measured at the centre of the Plexiglas plate. The pressure distribution was obtained by moving the plate with respect to the jet. In the centre of the plate plugs with pressure taps were flush mounted, either for measurements of pressure fluctuations using a microphone, or for mean-pressure measurements with a MKS Baratron pressure transducer. The sensing area of the 3.2 mm diameter Bruel and Kjaer condenser microphone was reduced by using a 0.25 mm diameter pinhole of 2 mm depth. The resonant frequency of the cavity in front of the microphone was way beyond the frequency range of interest. The sensitivity of the microphone and the cavity assembly was calibrated using a B & K Model 4220 pistonphone.

3. Experimental procedure and data processing

3.1. *Velocity and pressure measurements*

The velocity field of the wall jet was surveyed in an area extending radially from $r/D = 0.8$ to 1.6. At all radial positions, which were $0.1D$ apart, the PW probe was traversed normal to the plate in steps of 0.1 mm (±0.02 mm) from $z = 0.2$–1.1 mm and in increasingly coarser steps at a larger wall distance z.

For data acquisition and processing, including the hot-wire calibration, a PDP 11/55 minicomputer was used. For the velocity measurements the two PW probe signals, the speaker signal and the pressure in the jet stagnation chamber were

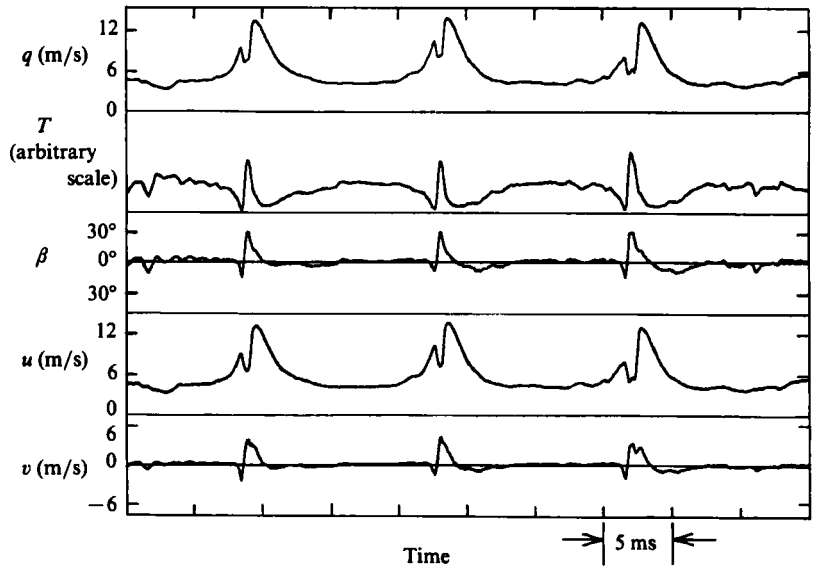

FIGURE 4. Time traces of total velocity q and temperature fluctuations T. The flow angle β and velocity components u and v are computed from q and T. (Example at $r/D = 1.1$, $z = 1.3$ mm.)

digitized at 0.1 ms intervals for 1 s (70 s periods). At the 10 kHz sampling rate 142 time-steps per period were available for phase averaging and the smallest periodic structure in the separated flow (maximum frequency about 2 kHz) was well resolved.

As mentioned in § 2.3 the frequency response of the second wire sensing the wake temperature had a first-order low-pass-filter characteristic with a corner frequency of 700 Hz. A digital frequency compensation of the output signal was performed by multiplying the signal in the frequency domain first with the inverse transfer function of a low-pass filter with corner frequency 700 Hz and then with the transfer function of a low-pass filter with corner frequency 3.5 kHz. Thus the frequency compensation shifted the corner frequency of the response function of the second wire from 700 Hz to 3.5 kHz.

The data were further processed in the following steps: (1) computation of velocity $q(t)$ and flow angle $\beta(t)$ using the calibration function; (2) computation of velocities $u(t)$ and $v(t)$; (3) computation of phase averages $\hat{u}$ and $\hat{v}$ by conditional sampling, which is described in the next section. As an example signals obtained at the radial location $r/D = 1.1$ in the outer part of the boundary layer are shown in figure 4. The peaks of the q- and u-signals corresponded to the passage of ring vortices in the shear layer of the wall jet. The regularity of the signal provided evidence that the flow field of a single event could be represented by ensemble averaging. The mean and the fluctuating wall pressure was measured at radial positions ranging from the stagnation point to $r/D = 1.8$, with a minimum stepsize of $r/D = 0.025$ near separation. The microphone output signal and the speaker signal as phase references were digitized at 0.1 ms intervals over 2 s (140 periods). Phase averages of the fluctuating pressure were computed and then the mean pressure was added at each radial station to obtain the phase-averaged total pressure p.

3.2. *Conditional sampling*

For computing phase averages in a periodically forced flow the forcing signal of period $T = 1/f$ could be used as a detector for sampling. Here the phase $t/T = 0$ was arbitrarily defined as the negative-to-positive zero-crossing of the speaker signal. However, when the speaker voltage was used as a sampling condition, the small-scale structure of the velocity signal was slightly blurred owing to phase fluctuations of the ring vortices having travelled several wavelengths from the jet nozzle to the measuring location. Therefore, characteristic features of the velocity signal itself were chosen as the sampling condition: those features were either the sharp minimum of v-velocity near the separated region or the extremum of u-velocity during vortex passage. A further selection criterion was provided by the phase reference. The phase relative to the zero-crossing of the speaker signal t_i/T of each ensemble at the chosen sampling characteristic feature was registered. The average phase $\bar{t}/T$ of all realizations were computed. The symbols with an over-bar $\bar{}$ represent the long-time-averaged values. For ensemble averaging only those realizations with a phase deviation $(t_i - \bar{t})/T \leqslant 0.028$ (5 time steps) were used. This method eliminated parts of the signal with either large phase fluctuations or with time marks set incorrectly owing to a distorted signal shape. Between 40 and 50 realizations contributed to the phase averages $\hat{u}$ and $\hat{v}$. The symbols with $\hat{}$ stand for the phase-averaged properties. The phase relation between the signals from different spatial points was provided by the average phase $\bar{t}/T$ at each measuring location.

The same procedure was applied for computing phase averages of the wall-pressure signal. For $r/D \leqslant 0.9$ the zero-crossing of the pressure signal and for $r/D > 0.9$ the negative pressure peak were used as the sampling condition. The pressure was typically averaged over 80 realizations.

The data presented in this paper are spline-fitted. Examples of measured data are plotted in figures 6 and 10(a) which show the amount of scatter.

4. The flow field

4.1. *Visualization*

The smoke visualization (figure 5) provided an overall view of the flow field. The photos taken with an exposure time of 18 periods gave an idea of the repeatability of the ring vortices: the natural jet instability and much of the background fluctuations were suppressed by forcing. In the first photo (figure 5a) the primary vortex was still approaching the wall and the boundary layer was attached. A short fraction of the period later (figure 5b) the boundary layer was separated and the concentration of smoke in the separated region suggests that a secondary vortex of circulation opposite to the primary vortex was already formed slightly downstream of the primary vortex. The separation location moved downstream of the primary vortex. The separation location moved downstream with the primary vortex, and the secondary vortex lifted off from the plate (figure 5c) and finally was wrapped around the primary vortex. Further downstream the ring vortex disintegrated. The disintegration might have been caused by an azimuthal instability (Didden 1977; Widnall & Tsai 1977). In the case of an isolated impinging ring vortex azimuthal waves were found to start on the circumference of the secondary vortex (Cerra & Smith 1980). In the initial region of separation the flow visualization showed that azimuthal corrugation was negligible and the flow could be considered axisymmetric.

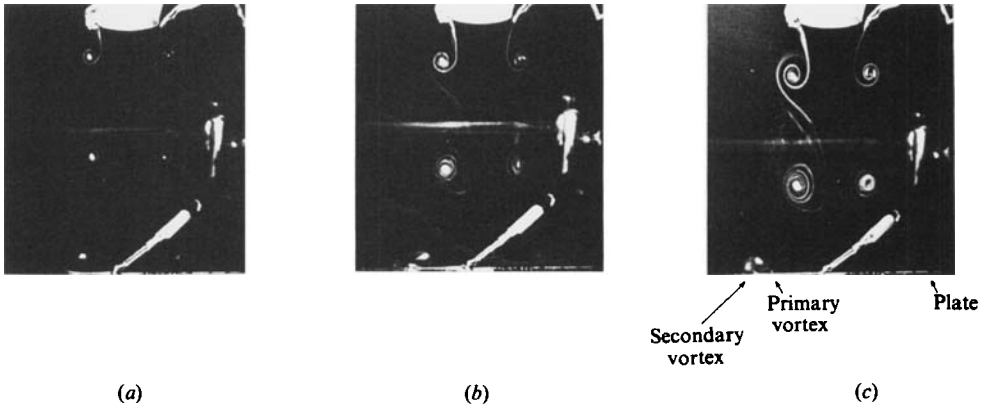

FIGURE 5. Smoke visualization of forced jet ($f = 70$ Hz) and of boundary-layer separation in stroboscopic illumination. Exposure time 18 periods, $18T = 18/f$. $U_0 = 7.5$ m/s: (*a*) $t/T = 0.12$; (*b*) 0.24; (*c*) 0.33.

4.2. *Time-averaged velocity*

Profiles of the time-averaged velocity $\overline{U}(z)$ are plotted in figure 6 *versus* the non-dimensional wall distance z/z_1. The time-averaged displacement thickness $z_1 = \bar{\theta}_d = 0.25$ mm at the radial position $r/D = 0.9$ was chosen as the lengthscale for normalization: at $r/D = 0.9$ the flow was still attached. The maximum streamwise velocity at the edge of the laminar boundary layer increased from the stagnation point to $r/D = 1.0$. Further downstream the maximum value decreased and the boundary-layer thickness increased. The flattening of the velocity peak at $r/D > 1.1$ was caused by separation during a short fraction of each cycle. This will become obvious from the phase-averaged-velocity profiles. The mean profiles at a wall distance $z/z_1 > 8$ became flat at $r/D \geqslant 1.5$ where the secondary vortex was lifted off from the plate and wrapped around the primary ring vortex.

Large negative values of the normal velocity $\overline{V}$ in the impinging jet region $r/D \leqslant 1.0$ indicated flow towards the wall (figure 7). The positive $\overline{V}$ at $r/D = 1.0$, 1.1 near the solid surface indicated the separation zone. Further downstream and outside of the boundary layer at a wall distance $z/z_1 < 20$ the time-averaged velocity towards the wall was small with typical values $\overline{V} = -0.05\overline{U}$ corresponding to flow angles $\beta = -3°$. In the path of the primary ring vortices at $z/z_1 > 20$ the large negative $\overline{V}$-velocity might be an indication for entrainment of fluid into the wall jet enhanced by the passing ring vortices. However, because of large angles near the vortex core, the angle measurements with the PW probe in this region could not be considered very accurate. We are concerned here only with the separation taking place near the wall and thus the flow within the primary ring vortices was not investigated further, except for the determination of the convection speed of the vortex core.

4.3. *Convection speed and phase-averaged velocity*

The convection speed of the primary-vortex core moving along the plate in the radial mean-flow direction was derived from the vortex passage time t_v/T at each radial measuring position: the phase-averaged time traces of the magnitude of the velocity vector $q(t)$ through the vortex core exhibited a characteristic V-shaped minimum which allowed us to determine the passage time t_v/T with an estimated error of $\Delta t_v/T = 0.01$ (figure 8). In the range $r/D = 0.8$–1.4 the convection speed U_c of the

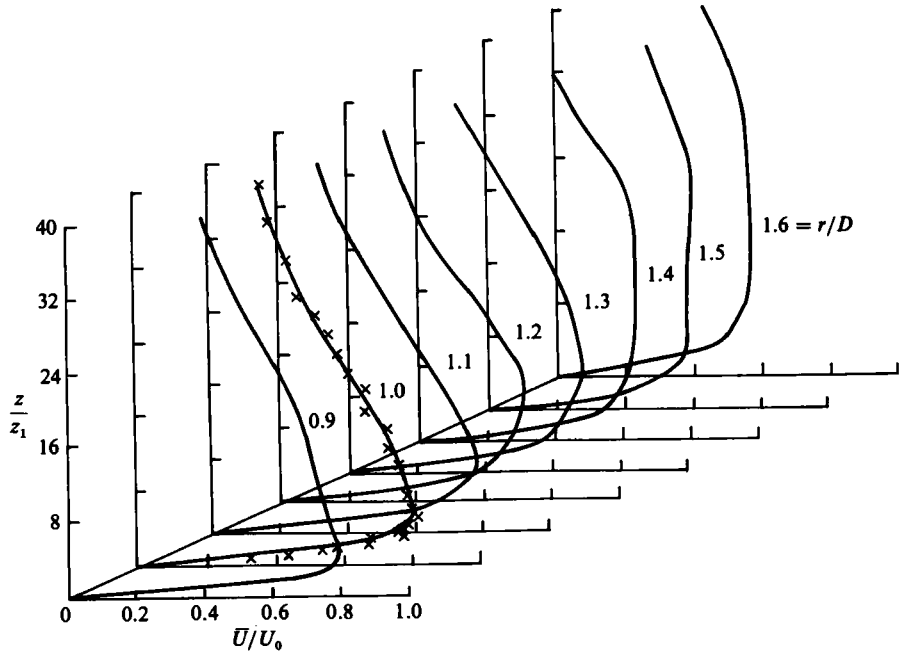

FIGURE 6. Time-averaged-velocity profiles $\bar{U}(z)$ of the wall jet at various radial positions, r/D. $U_0 = 7.5$ m/s, $z_1 = 0.25$ mm. ×, example of measured data points showing the amount of scatter from the spline-fitted curve.

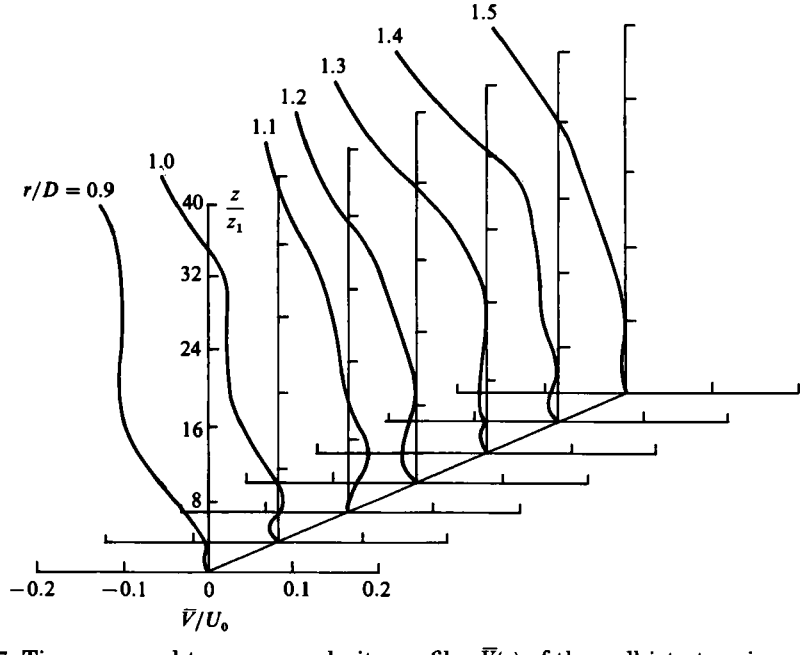

FIGURE 7. Time-averaged transverse-velocity profiles $\bar{V}(z)$ of the wall jet at various radial positions, r/D. $U_0 = 7.5$ m/s, $z_1 = 0.25$ mm.

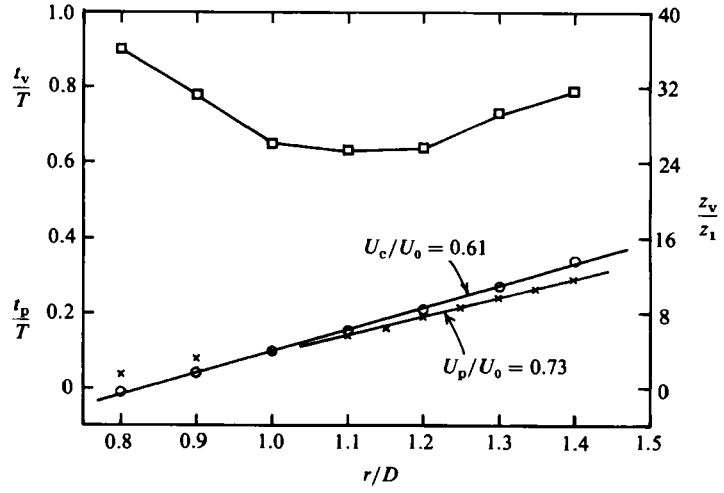

FIGURE 8. Passage-time t_v/T and wall distance z_v/z_1 of the primary vortex axis *versus* radial distance r/D. t_p/T is passage time of negative wall-pressure peak. □, z_v/z_1; ○, t_v/T; ×, t_p/T.

vortex was found to be constant: $U_c = 0.61U_0$. At larger radial distances the vortex-core position was no longer well defined owing to the spatial jitter introduced by the interaction between the primary vortex and the secondary vortex. It is interesting to note that the convection speed of the primary vortex in the wall jet was the same as that in the jet shear layer before impingement: from flow visualization the spacing (wavelength λ) between the ring vortices was found to be $\lambda/D = 1.7$, yielding a convection speed $\lambda f = 0.6U_0$. The same value was measured in the free jet.

The distance z_v of the primary vortex axis from the wall (figure 8) was determined by the z-position, at which the velocity $q(z, t_v)$ at the passage time t_v was equal to the convection velocity U_c. In the range $r/D < 1.0$, the ring vortices approached the wall. From $r/D = 1.0$–1.2 they moved almost parallel to the wall at a distance $z_v/z_1 \geqslant 25$.

In the three-dimensional plot (figure 9) the time traces $\hat{u}(t/T)$ were cross-plotted *versus* z at constant phase t/T. At all radial positions the broad velocity peak was due to the passage of the ring vortex in the outer flow at a wall distance $z_v/z_1 \geqslant 25$ (see figure 8). At $r/D = 0.9$ the values of the $\hat{u}(z)$-profiles at the outer edge of the boundary layer varied from $\hat{u}_{max} = 1.6U_0$ at the time of vortex passage to $\hat{u}_{max} = 0.45U_0$ between two vortices. At $r/D = 1.0$ for the first time an inflection point in the velocity profile that was slightly ahead of the vortex appeared at $t < t_v$. At $r/D = 1.1$ and 1.2 the velocity defect ahead of the vortex became very pronounced. The defect of the streamwise velocity was associated with a sixfold increase in the positive maximum normal velocity $\hat{v}_{max}$ from $r/D = 0.9$–1.2 ($\hat{v}_{max} = 0.8$–5.0 m/s).

In figure 10 the temporal development of the $\hat{u}(z)$-profiles during the vortex passage is shown in more detail: at $r/D = 1.0$ the velocity near the wall substantially decreased between $t/T \approx 0$ and 0.05. One measuring location further downstream, at $r/D = 1.1$, the first zero velocity gradient $\partial\hat{u}/\partial z$ appeared slightly before $t/T = 0.075$. Negative velocity gradients within the boundary layer appeared from t/T 0.075–0.0125. At $t/T = 0.15$ zero $\partial\hat{u}/\partial z$ was clearly detected again. The significance of $\partial\hat{u}/\partial z = 0$ for separation will be discussed in a later section together with other features indicating separation.

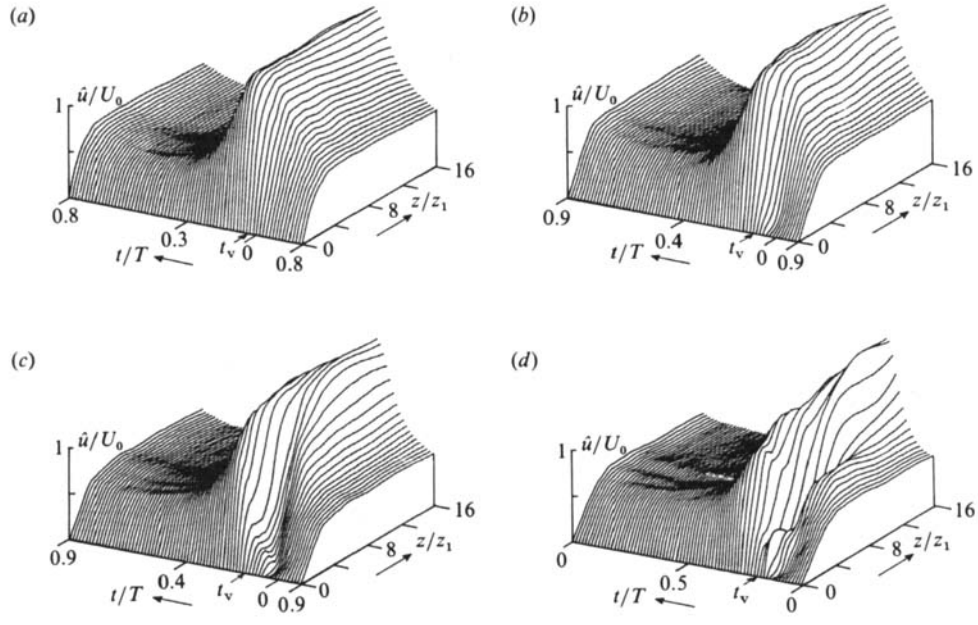

FIGURE 9. Phase-averaged velocity profiles $\hat{u}(z)$ of the wall jet boundary layer *versus* phase t/T. t_v is the passage time of the primary vortex axis at each radial position: (*a*) $r/D = 0.9$, (*b*) 1.0, (*c*) 1.1, (*d*) 1.2.

4.4. *Thickness of unsteady boundary layer*

The influence of separation and subsequent secondary-vortex formation upon the boundary-layer thickness is demonstrated by computing the phase-averaged displacement thickness

$$\hat{\theta}_d\left(\frac{t}{T}\right) = \int_0^{z_{max}} \left(1 - \frac{\hat{u}(z, t/T)}{\hat{u}_{max}(t/T)}\right) dz$$

with $z_{max} = z(\hat{u}_{max}(t/T))$ being the boundary of the internal flow. A plot of $\hat{\theta}_d$ *versus* radial distance r/D interpolated by a cubic spline function is shown in figure 11 at several phases t/T. At $r/D = 0.9$ the variation of $\hat{\theta}_d$ over one cycle was small although the velocity $\hat{u}_{max}$ at the edge of the boundary layer varied considerably, as seen from figure 7 (*a*). The flow is not separated here. The time-averaged displacement thickness $z_1 = \hat{\theta}_d$ at this position was considered to be the lengthscale of the non-separated boundary layer and was used for normalizing the wall distance. The time-averaged displacement thickness $\hat{\theta}_d$ increased monotonically with r/D. At each radial position the thickening of the boundary layer took place over a short fraction of the period only, with a minimum value of $\hat{\theta}_d$ at the time between two vortex passages being approximately equal to z_1. At $r/D = 1.1$ the displacement thickness varied by a factor 4 over each cycle. At this position the boundary layer was already separated, as we shall see later. The maximum of $\hat{\theta}_d$ moved downstream ahead of the ring vortex and increased in magnitude as the secondary vortex increased in size. The absolute maximum of $\hat{\theta}_d = 18z_1$ was reached at $r/D = 1.5$. At this radial position, the secondary vortex was wrapped around the primary vortex. A reduction of the displacement thickness started at $r/D = 1.6$.

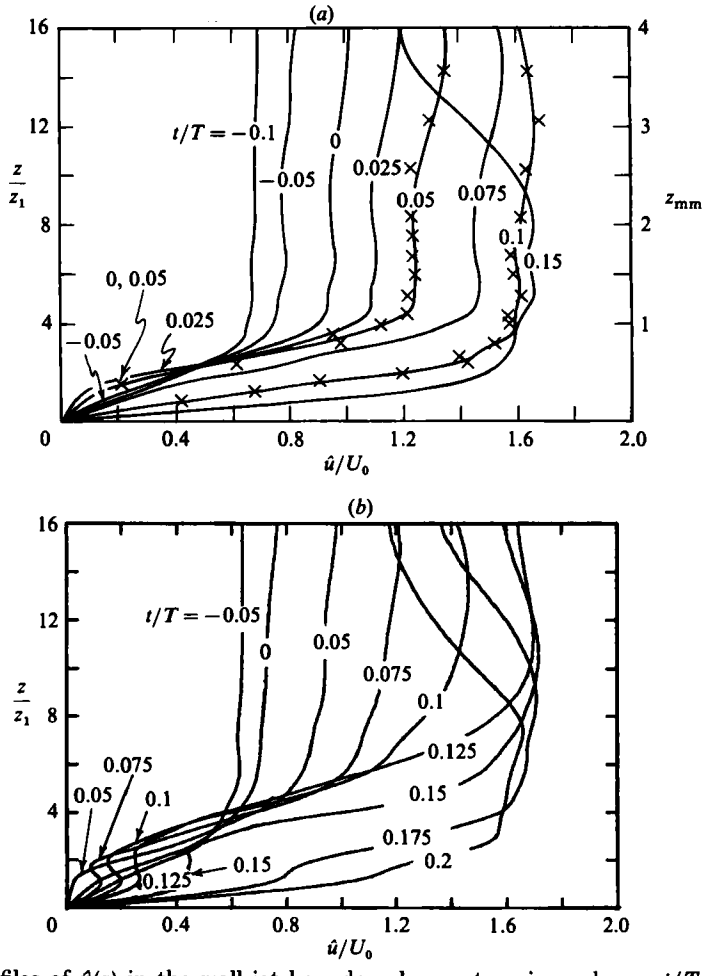

FIGURE 10. Profiles of $\hat{u}(z)$ in the wall-jet boundary layer at various phases, t/T during vortex passage: (*a*) $r/D = 1.0$, (*b*) 1.1. ×, example of measured data points showing the amount of scatter from the spline-fitted curve.

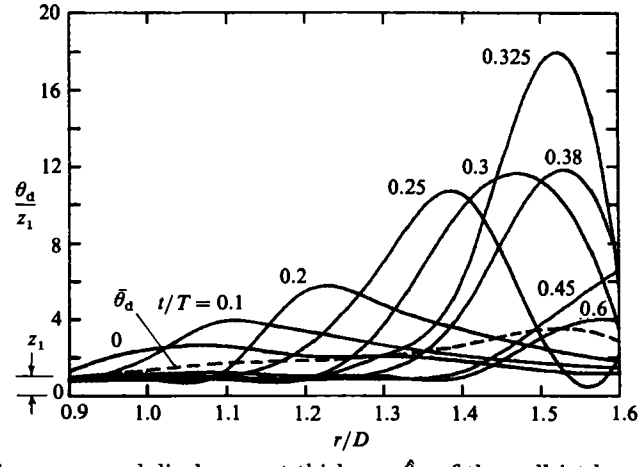

FIGURE 11. Phase-averaged displacement thickness $\bar{\theta}_d$, of the wall-jet boundary layer *versus* radial distance r/D at various phases t/T.

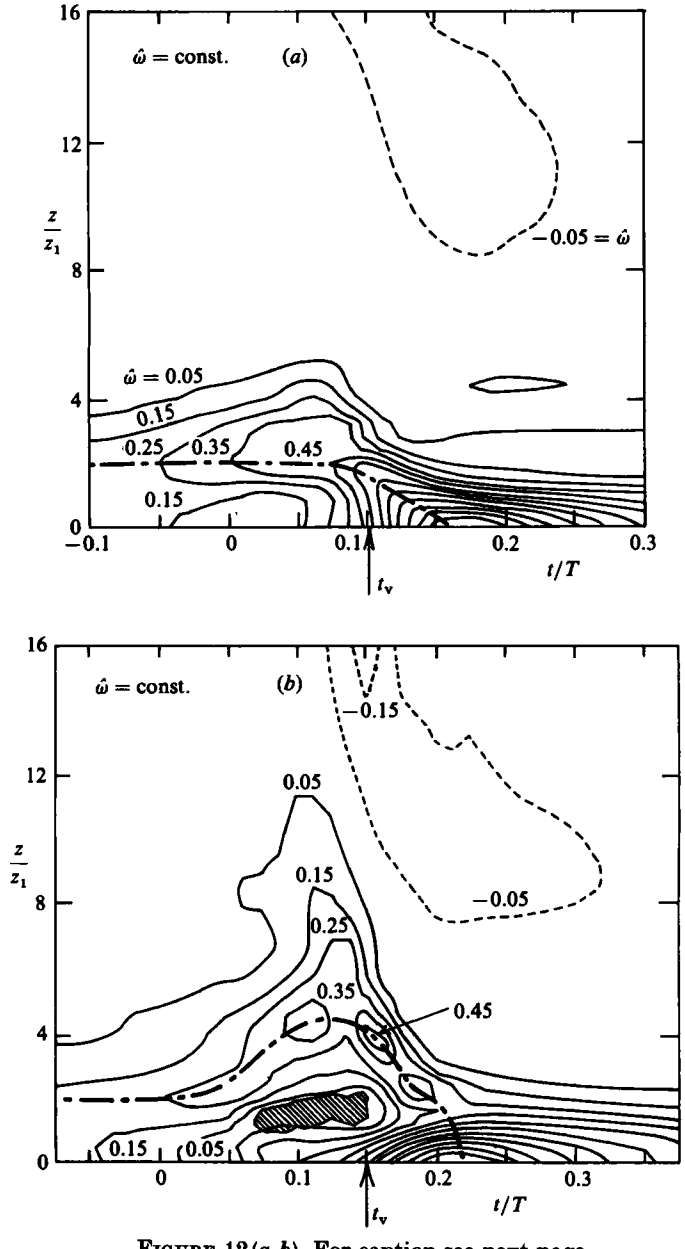

FIGURE 12(*a*,*b*). For caption see next page.

4.5. *Temporal development of vorticity and zero shear stress*

In the unsteady separated flow the temporal development of vorticity and zero shear stress at several spatial stations near the separated region were very revealing. The phase-averaged azimuthal component of the vorticity was defined as

$$\hat{\omega} = \frac{\partial \hat{u}}{\partial z} - \frac{\partial \hat{v}}{\partial r}.$$

In figure 12 contours of constant vorticity, normalized with U_0/z_1, are plotted at three

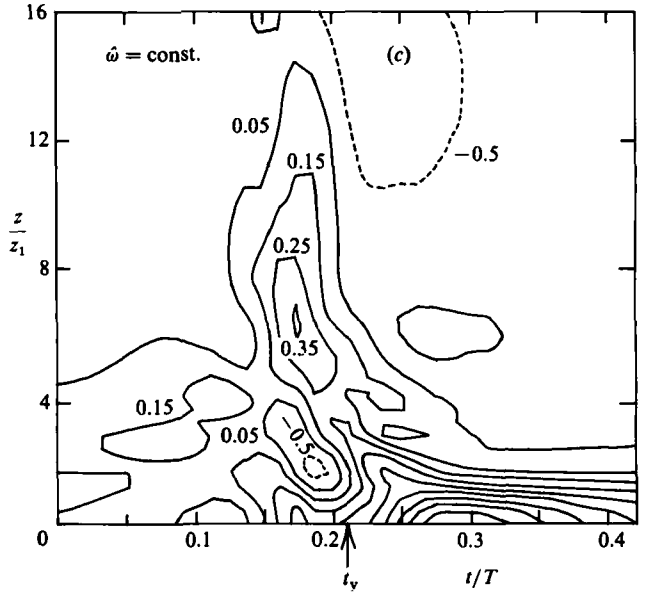

FIGURE 12. Contours of constant vorticity: ——, positive-vorticity contour; ----, negative-vorticity contour; – ·–, maximum $\hat{\omega}$. (*a*) $r/D = 1.0$; (*b*) 1.1 (shaded area is the boundary of negative phase-averaged stress); (*c*) 1.2.

locations, $r/D = 1.0$, 1.1 and 1.2, during the half cycle when the flow separated (figure 12). The derivative $\partial/\partial r$ was approximated by $-1/U_c(\partial/\partial t)$. U_c was the convection speed of the primary vortex and equalled $0.61U_0$. This approximation introduced a distortion, because the flow pattern did not convect with a uniform velocity. However, $\partial\hat{v}/\partial r$ usually was much smaller than $\partial\hat{u}/\partial z$ and thus the distortion was not very appreciable.

At all radial positions the vortex passage was associated with a vorticity maximum at the wall. At $r/D = 1.0$ boundary-layer vorticity tended to lift off from the wall. At $r/D = 1.1$ for the first time a local vorticity maximum away from the wall was observed at $z/z_1 = 4$ and appeared at the same time t_v as the primary vortex passed this location. The vorticity maximum had an opposite sign to the primary vortex and presumably was the induced secondary vortex. At $r/D = 1.2$ the ejected vorticity protruded further into the outer flow and the vorticity maximum was detected prior to the passing of the primary vortex. The fact that the secondary vortex moved faster than the primary vortex agreed with the visualization result.

The phase-averaged shear stress is defined as

$$\hat{\tau} = \mu\left(\frac{\partial\hat{u}}{\partial z} + \frac{\partial\hat{u}}{\partial r}\right).$$

Close to the wall the lines of constant shear stress almost coincided with the vorticity contours, since $\partial\hat{v}/\partial r \ll \partial\hat{u}/\partial z$. At the three radial locations (figure 12), the wall shear stress was found to be positive throughout the period. Thus the zero wall shear stress, which defines the steady separation point, did not exist in this unsteady flow. However, zero shear stress was detected away from the wall as is indicated by the boundary of negative shear stress (the shaded area in figure 12*b*).

5. Onset of unsteady separation

5.1. *Symptoms of unsteady separation*

The measured spatial (figure 9) and temporal evolution (figure 12) of the velocity field provides a clear picture of the unsteady separation process and shows a sequence of separation symptoms, namely the thickening of the boundary layer, ejection of vorticity, zero shear stress, etc. These phenomena will be examined quantitatively from the detailed documentation of flow properties. The symptoms were detectable at $r/D = 1$, but not at $r/D = 1.0$, which is about 4 mm upstream. The flow properties at these positions can offer tremendous insight into the unsteady-separation process.

The thickening of the boundary layer did occur in the unsteady separated flow. The maximum phase-averaged boundary-layer thickness at $r/D = 1.5$ (figure 11) was not an indication of the initial phase, but rather of the climax of separation. At $r/D = 1.0$ a slight variation of the thickness was observed. An abrupt change of the boundary-layer thickness, but still much milder than that at $r/D = 1.5$, clearly existed at $r/D = 1.1$. The peak value of $\hat{\theta}_d$ was about $4z_1$ at this location. The constant-vorticity contours also confirmed this (figure 12*b*). The thickening of the boundary layer was a convective phenomenon (figure 11). The convection speed of the peak $\hat{\theta}_d$ at $r/D = 1.1$ was about $0.4U_0$.

In the viscous flow the solid boundary was a source of vorticity. The passing primary vortex induced a local shear flow away from the wall. The local shear layer, located around the vorticity maximum and shown by the thick broken line in figure 12(*a*), had an *opposite* sign to the primary vortex and exists *before* the separation. *The shear layer was unstable.* The vorticity lumped together (figure 12*b*) and eventually formed the secondary vortex. The process of vortex formation is similar to that in a free shear layer (Brown & Roshko 1974; Ho & Huerre 1984) but the detailed process could be affected by the wall. The local shear layer also occurred immediately before the separation of an impulsively started cylinder (Van Dommelen & Shen 1982). We believe that *the local shear layer is the generic flow module in the unsteady separation phenomenon* (Ho 1983). The induced secondary vortex counter-rotates with respect to the primary vortex as was observed in the flow visualization. The secondary vortex first appeared at the passage time of the primary vortex (t_v in figure 12*b*) and was convected at a speed of $0.73U_0$. While the secondary vortex moved downstream, it moved ahead of the primary vortex (figure 12 *c*) and ejected away from the wall.

The first zero shear stress was detected slightly before $t/T = 0.075$, the local velocity $\hat{u}/U_0$ was 0.1. The velocity profile then evolved into an S-shaped profile which had two points of zero shear stress with two different local velocities. Finally, the local velocity at the shear stress became single-valued again and was about 40% of U_0. We should stress that the thickness of the boundary layer was maximum at this moment, $t/T = 0.15$.

5.2. *Criteria of unsteady separation*

The criterion of unsteady separation has been a controversial topic for some time. The qualitative criteria, i.e. the symptoms described in §5.1, did occur in separated flow, but they appeared at different times and convected at different speeds. In other words these qualitative descriptions were all associated with the separation process, but were not equivalent to each other. Hence controversy was introduced. Furthermore, the lack of a well-documented flow field accentuated the problem. The main problem of the quantitative criterion, the MRS criterion, is the 'separation velocity' which is not known *a priori*. There are many velocity scales in the present flow field;

the jet exit velocity (U_0); the convection velocity of the primary vortex ($0.61U_0$); the convection velocity of the ejected vortex ($0.73U_0$); the convection velocity of the peak $\hat{\theta}_d$ ($0.4U_0$); and the velocity at the zero-shear-stress point.

However, an especially interesting situation occurs when the thickness of the boundary layer reaches maximum. At this moment the boundary-layer assumption breaks down owing to the large transverse gradient. The phase-averaged velocity ($t/T = 0.15$) in figure 10(*b*) evolves into the Moore's-type downstream-moving profile (figure 1). The local velocity at zero shear stress is about $0.4U_0$, which is the same as the convection speed of the peak $\hat{\theta}_d$. If this velocity is chosen as the 'separation' velocity, the MRS criterion for downstream-moving separation is validated. At this location ($r/D = 1.1$) the phase-averaged streamlines are found to form a closed recirculation region (Ho 1983). This feature qualitatively agrees with Walker's (1978) calculation for a line vortex near a wall.

6. Mechanism of unsteady separation

6.1. *Wall pressure*

The radial distribution of mean gauge pressure $\bar{P}(r)$ and the mean pressure gradient $\partial\bar{P}/\partial r$, normalized with the pressure in the jet stagnation chamber P_0, are shown in figure 13. In the stagnation region of the impinging jet the mean pressure dropped by about 50% from the stagnation point to $r/D = 0.6$, where the mean pressure gradient reached a minimum. At $r/D = 1.0$ the mean pressure was about 10% of the stagnation pressure. The mean pressure gradient was favourable everywhere.

The pressure fluctuations p' were of the same order of magnitude as the mean pressure. The resulting total phase-averaged pressure $\hat{p} = \bar{p} + p'$ at several radial positions is presented in figure 14. At the stagnation point the pressure variation was almost sinusoidal. Further downstream at $r/D \geqslant 0.8$ the pressure became negative in the low-pressure regions corresponding to high-velocity regions of the passing vortices. In the range $r/D > 1.0$–1.4 a characteristic negative pressure peak became the dominant feature of the time trace. The data of the phase-averaged pressure were cross-plotted in figure 15 as a function of radial distance. Pressure fluctuations were very large near the beginning of the separation and became much reduced in magnitude near the climax of the separation, $r/D = 1.5$. The passage time of the pressure minimum t_p/T, versus radial distance was plotted in figure 8. At $r/D \geqslant 1.1$ the convection velocity of the negative pressure peak was found to be $U_p = 0.73U_0$, which is 20% higher than the primary vortex convection speed U_c. The ejected vorticity, the second vortex, also convected at the same speed, $0.73U_0$.

In figures 14 and 15 fairly clear changes of the slopes were observed in the pressure traces near the separated region, $1.0 < r/d < 1.5$, and were indicated by arrows. The pressure fluctuations seemed to be composed of a smooth and low-amplitude portion as well as a sharp and high-amplitude portion. The smooth part of the low-pressure regions were associated with the high-velocity regions of the passing primary vortex. For the following two reasons we conjectured that the high-amplitude pressure fluctuations were caused by the unsteady separation rather than by the primary vortex. First, the high negative peak pressure appeared at about the same time as the secondary vortex (figures 12 *c* and 14) and travelled with a speed of $0.73U_0$, which is equal to the speed of the secondary vortex, but 20% higher than that of the primary vortex. Secondly, in the range $r/D = 1.0$–1.2 the primary vortex moved almost parallel to the wall (figure 8) and the maximum streamwise velocity at the outer edge

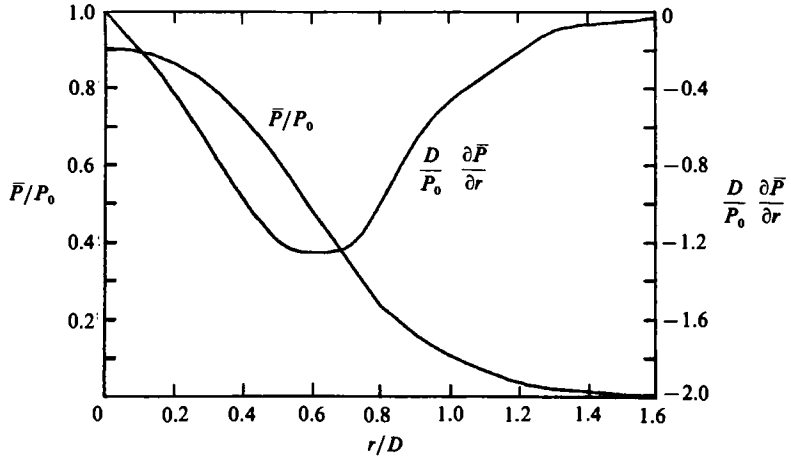

FIGURE 13. Radial distribution of time-averaged wall pressure $\bar{P}$ and pressure gradient $\partial p/\partial r$; P_0 is the mean pressure inside stagnation chamber.

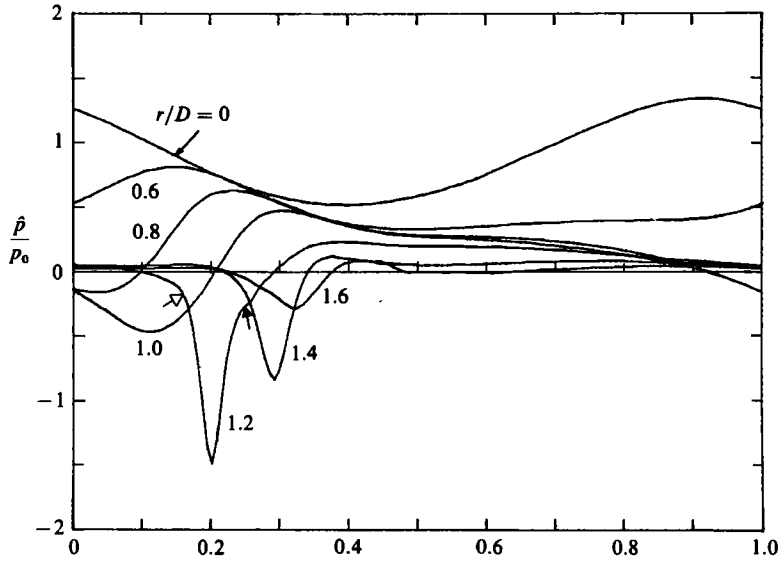

FIGURE 14. Phase-averaged wall-pressure signal $\hat{p}$ over one cycle at various radial positions r/D. The arrows indicate the sudden change of the slope (§6.1).

of the boundary layer was approximately constant (figure 9). Hence, over this range the peak pressure induced by the passing primary vortex was not expected to change. The negative pressure peak, however, increased by a factor of 3 from $r/D = 1.0$ to 1.2.

While studying the feedback loop in a resonating impinging jet Ho & Nosseir (1981) detected a high-pressure-fluctuation region near $r/D = 1.0$ and took that location as the reference point of the feedback loop. Apparently the large pressure fluctuations were caused by the unsteady separation. The surface fluctuating pressure radiated from the wall and produced the feedback acoustic waves. A similar vortex-induced separation can be observed in the jet impinging on a wedge (Tang & Rockwell 1983; Homa & Rockwell 1983). It is expected that the high-level pressure fluctuations will also occur at the unsteady separation location and functions as the source of the

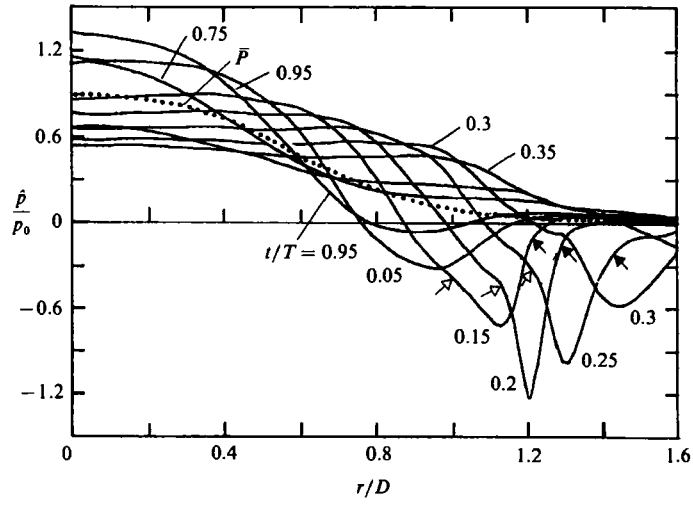

FIGURE 15. Radial distribution of phase-averaged wall pressure $\hat{p}$ at various phases t/T. The arrows indicate the sudden change of the slope (§6.1).

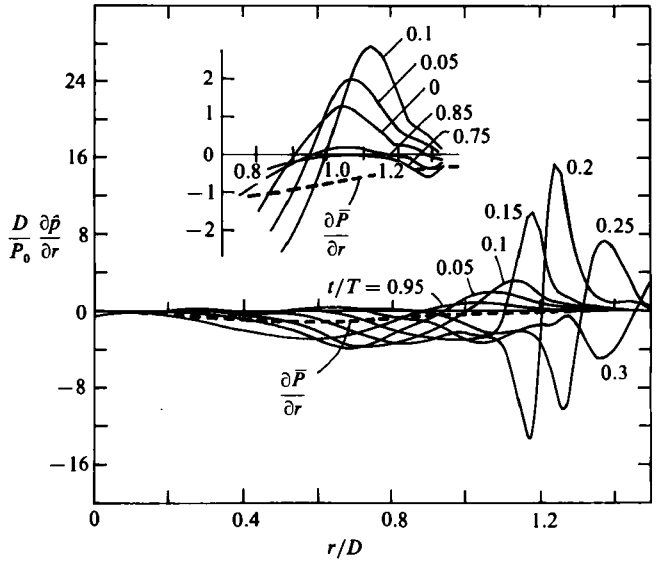

FIGURE 16. Radial distribution of phase-averaged wall-pressure gradient $\partial\hat{p}/\partial r$ at various phases t/T.

feedback to produce the edge tone. The lengthscale in the edge-tone phenomenon should then be measured from the jet exit to the separation location rather than the conventional one, which is the distance between the jet and the tip of the wedge.

6.2. *Unsteady pressure gradient*

At each instant the unsteady flow experiences the unsteady pressure gradient and changes its velocity accordingly. The mean pressure gradient is simply a long-time-averaged value and does not adequately indicate the instantaneous flow. The phase-averaged pressure gradient is shown in figure 16. For $r/D < 0.9$ the pressure

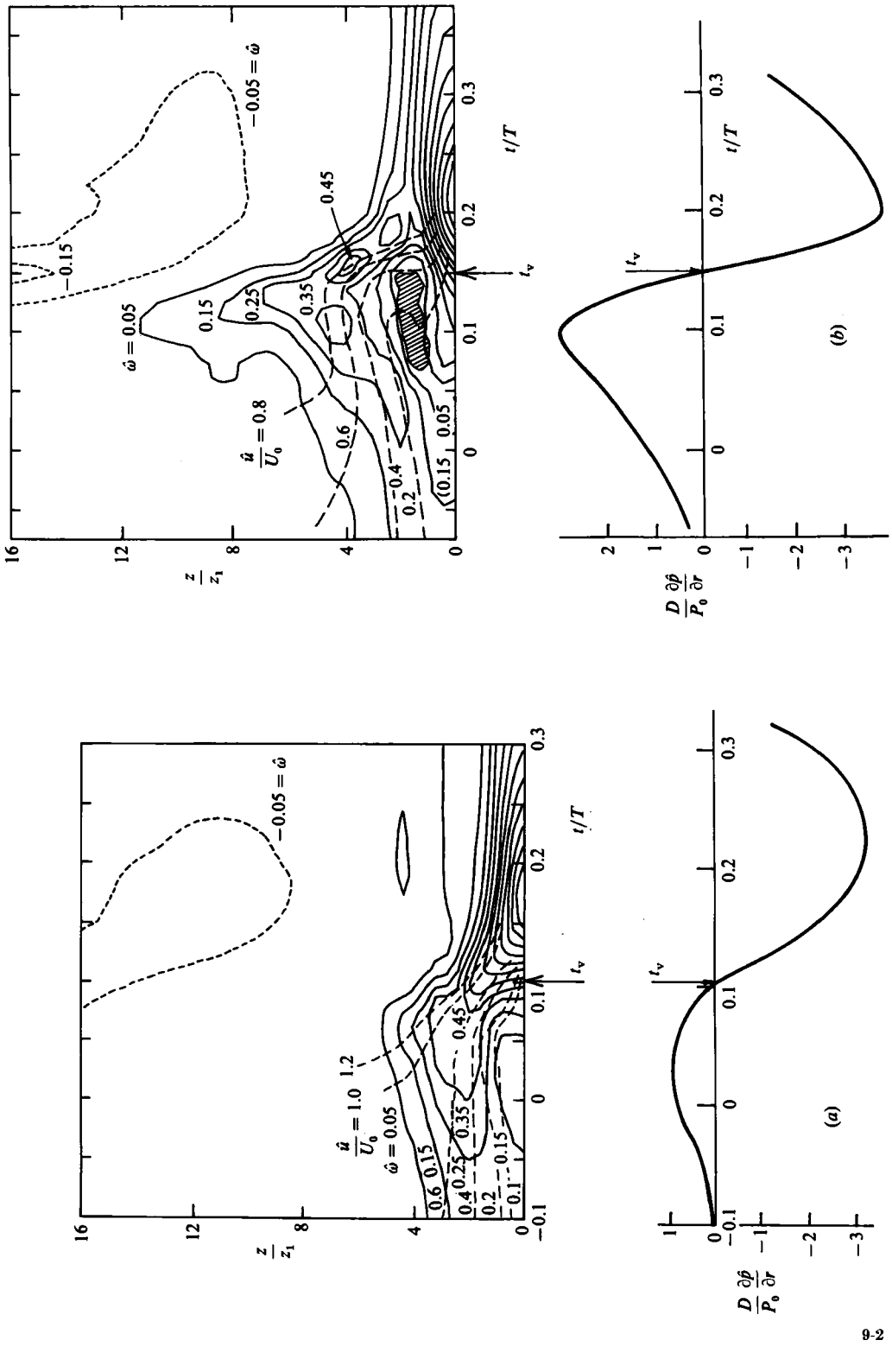

FIGURE 17. Unsteady spatial pressure gradient and the temporal variation of the velocity and vorticity field: (*a*) $r/D = 1.0$; (*b*) 1.1.

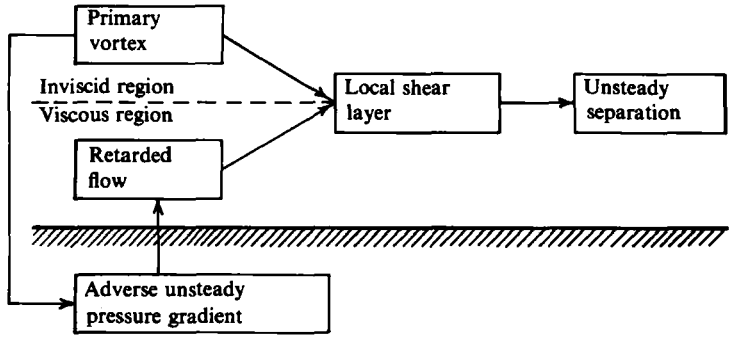

FIGURE 18. Viscous–inviscid interaction.

gradient was always favourable. Adverse pressure gradients occurred downstream of $r/D = 0.9$ and reached the maximum value near $r/D = 1.2$. The sharp peaks of $\partial\hat{p}/\partial r$ near $r/D = 1.2$ were generated by the separation. The interesting part is the unsteady adverse pressure gradient (the enlarged portion in figure 16) *before* the onset of the unsteady separation ($r/D = 1.1$ and $t/T = 0.15$). This level of the unsteady adverse pressure gradient was generated by the primary vortex not by the separation. The flow experienced the large adverse pressure gradient at $r/D = 0.9$ and started to decelerate. Eventually, the flow separated at $r/D = 1.1$. Apparently, *the unsteady adverse pressure gradient is the mechanism leading to the unsteady separation.*

6.3. *Viscous–inviscid interaction*

In general the separation phenomenon involves both the viscous and inviscid flows. In many cases the perturbations from the inviscid region cause the fluid in the viscous region to separate from the wall. The ejected fluid protrudes into the inviscid region and changes the global properties. The present study serves as a good example to explain some aspects of the viscous–inviscid interaction.

The primary vortex induced an unsteady adverse spatial pressure gradient before the pass of the vortex ($t < t_v$ in figure 17*a*). The wall-pressure gradient changed sign at $t = t_v$. The dashed lines show the contours of constant velocity. At a constant value of z the flow temporally decelerates for $z/z_1 < 3$ and accelerates in the outer region before the passing of the primary vortex. For $z/z_1 < 3$ the phase-averaged velocity profiles at $r/D = 1.0$ (figure 10*a*) show high velocity gradients which indicate a strong viscous effect. Hence the flow in the *viscous* region is retarded by the unsteady adverse pressure gradient for $t < t_v$. At the same time interval the flow accelerates in the *inviscid* region ($z/z_1 > 3$). A *local shear layer* with vorticity having a sign opposite to that of the primary vortex forms at the boundary of the inviscid and viscous zones. The local shear layer has an inflectional velocity profile and is unstable. In the case of a shear layer free from the wall interference the flow is *inviscidly* unstable. The fast-growing stability waves roll up into vortices (Ho & Huerre 1984). At this time, the vorticity in the local shear layer also lumps into a counter-rotating vortex in a short distance (figure 17*b*). The vortex lifts up from the wall and originates the unsteady separation. Nishioka, Asai & Iida (1980) studied the instability of an inflectional velocity profile near a wall. They found that the stability process is similar to that of a free shear layer. The viscosity does not play an important role. However, the viscous effect is essential for producing the shear layer before the onset of the unsteady separation.

7. Conclusion

In an impinging jet, the detailed documented velocity and wall pressure fields have revealed fundamental aspects pertinent to the laminar unsteady separation which occurs in the wall jet boundary layer. The *unsteady wall pressure gradient* produced by the perturbations in the *inviscid* region retards the flow in the *viscous* region. A *local shear layer* forms at the viscous–inviscid interface (figure 18). The vorticity in the shear layer lumps into a vortex and protrudes into the inviscid region. Thus the unsteady separation starts.

This work is supported by Air Force Office of Scientific Research Contract F49-620-82-K-0019. The authors appreciate the review of the final manuscript by Professor F. K. Browand.

REFERENCES

BROWN, G. L. & ROSHKO, A. 1974 On density effects and large structure in turbulent mixing layers. *J. Fluid Mech.* **64**, 775–816.

CEBECI, T. 1982 Unsteady separation. In *Numerical and Physical Aspects of Aerodynamic Flows* (ed. T. Cebeci), pp. 265–77. Springer.

CERRA, A. W. & SMITH, C. R. 1980 Experimental observation of the interaction of a vortex ring with a flat plate. *Bull. Amer. Phys. Soc.* **25**, 1092.

COUSTEIX, J., HOUDEVILLE, R. & JAVELLE, J. 1981 Response of a turbulent boundary layer to a pulsation of the external flow with and without adverse pressure gradient. In *Unsteady Turbulent Shear Flows* (ed. R. Michel, J. Cousteix & R. Houdeville), pp. 120–144. Springer.

DESPART, R. A. & MILLER, J. A. 1971 Separation in oscillating laminar boundary-layer flows. *J. Fluid Mech.* **47**, 21–31.

DIDDEN, N. 1977 Untersuchung laminarer, instabiler Ringwirbel mittels Laser-Doppler-Anemometrie. *Mitt. aus dem MPI für Strömungsforschung und der AVANR.* 64 Göttingen.

DOLIGALSKI, T. L. 1980 The influence of vortex motion on wall boundary layers. Ph.D. thesis, Lehigh University, Penn. U.S.A.

GUTMARK, E. & HO, C. M. 1983 On the preferred modes and the spreading rates of jets. *Phys. Fluids* **26**, 2932–2938.

HARVERY, J. K. & PERRY, F. J. 1971 Flow field produced by trailing vortices in the vicinity of the ground. *AIAA J.* **9**, 1659–1660.

HO, C. M. 1983 An alternative look at the unsteady separation phenomenon. *Recent Advances in Aerodynamics* (ed. A. Krothapalli & C. A. Smith), pp. 165–178. Springer.

HO, C. M. & HUERRE, P. 1984 Perturbed free shear layers. *Ann. Rev. Fluid Mech.* **16**, 365–424.

HO, C. M. & NOSSEIR, N. S. 1981 Dynamics of an impinging jet. Part 1. The feedback phenomenon. *J. Fluid Mech.* **105**, 119–142.

HOMA, J. & ROCKWELL, D. 1983 Vortex–body interaction. *Bull Am. Phys. Soc.* **28**, 1365.

KOROMILAS, C. A. & TELIONIS, D. P. 1980 Unsteady laminar separation: an experimental study. *J. Fluid Mech.* **97**, 347–384.

LIANG, S., FALCO, R. E. & BARTHOLOMEW, R. W. 1983 Vortex ring/moving wall interactions: experiments and numerical modelling. *Bull. Am. Phys. Soc.* **28**, 1397.

MAGARVEY, R. H. & MCLATCHY, C. S. 1964 The disintegration of vortex rings. *Can. J. Phys.* **42**, 684–689.

MCCROSKEY, W. J., CARR, L. W. & MCALISTER, K. W. 1975 Dynamic stall experiments on oscillating airfoils. *AIAA Paper No.* 75–125.

MOORE, F. K. 1985 On the separation of the unsteady laminar boundary layer. In *Boundary-Layer Research* (ed. H. G. Gortler), pp. 296–310. Springer.

NISHIOKA, M., ASAI, M. & IIDA, S. 1980 An experimental investigation of the secondary instability. In *Laminar Turbulent Transition* (ed. R. Eppler & H. Fasel), pp. 37–46. Springer.

PARIKH, P. G., REYNOLDS, W. C., JAYARAMAN, R. & CARR, L. W. 1981 Dynamic behaviour of an unsteady turbulent boundary layer. In *Unsteady Turbulent Shear Flows* (ed. R. Michel, J. Cousteix & R. Houdeville), pp. 35–46. Springer.

PRANDTL, L. 1904 Über Flüssigkeitsbewegung bei sehr kleiner Reibung. In *Proc. III Intl Math. Congr. Heidelberg*, pp. 484–491.

ROTT, N. 1956 Unsteady viscous flow in the vicinity of a stagnation point. *Q. Appl. Maths* **13**, 444–451.

SCHNEIDER, P. E. M. 1980 Sekundärwirbelbildung bei Ringwirbeln und in Freistrahlen. *Z. Flugwiss.* **4**, 307–318.

SEARS, W. R. 1956 Some recent developments in airfoil theory. *J. Aero. Sci.* **23**, 490–499.

SEARS, W. R. & TELIONIS, D. P. 1971 Unsteady boundary layer separation. In *IUTAM Symp. on Recent Research on Unsteady Boundary Layers* (ed. E. A. Eichelbrenner), vol. 1, pp. 404–447.

SIMPSON, R. L. 1981 A review of some phenomena in turbulent flow separation. *Trans. ASME* I: *J. Fluids Engng* **103**, 520–533.

TANG, Y. P. & ROCKWELL, D. 1983 Instantaneous pressure fields at a corner associated with vortex impingement. *J. Fluid Mech.* **126**, 187–204.

TELIONIS, D. P. 1981 *Unsteady Viscous Flows*. Springer.

VAN DOMMELEN, L. L. & SHEN, S. F. 1982 The genesis of separation. In *Numerical and Physical Aspects of Aerodynamic Flows* (ed. T. Cebeci), pp. 293–311. Springer.

WANG, K. C. 1979 Unsteady boundary layer separation. *Martin MarietaLab. Rep.* TR-79-16C.

WALKER, J. D. A. 1978 The boundary layer due to rectilinear vortex. *Proc. R. Soc. Lond.* A **359**, 167–188.

WALKER, T. B. & BULLOCK, K. J. 1972 Measurement of longitudinal and normal velocity fluctuations by sensing the temperature downstream of a hot wire. *J. Phys.* E: *Sci. Instrum.* **5**, 1173–1178.

WEIDMAN, P. D. & BROWAND, F. K. 1975 Analysis of a simple circuit for constant temperature anemometry. *J. Phys.* E: *Sci. Instrum.* **8**, 553–560.

WIDNALL, S. E. & TSAI, C. Y. 1977 The instability of the thin vortex ring of constant vorticity. *Phil. Trans. R. Soc. Lond.* A **287**, 273–305.

WILLIAMS, J. C. 1977 Incompressible boundary-layer separation. *Ann. Rev. Fluid Mech.* **9**, 113–144.